



Porous core-shell $Ti_xSn_{1-x}O_2$ solid solutions with broad-light response: One-pot synthesis and ultrahigh photooxidation performance

Qinfen Tian^{a,b}, Wenkang Wei^a, Juguo Dai^a, Qianqian Sun^a, Jiandong Zhuang^{a,*}, Yi Zheng^b, Ping Liu^b, Mizi Fan^a, Lihui Chen^{a,*}

^a College of Materials Engineering, Fujian Agriculture and Forestry University, Fuzhou, 350002, China

^b State Key Laboratory of Photocatalysis on Energy and Environment, Research Institute of Photocatalysis, Fuzhou University, Fuzhou, 350002, China



ARTICLE INFO

Keywords:

$Ti_xSn_{1-x}O_2$ solid solutions
Porous core-shell microspheres
Ostwald ripening
Broad-light responsive
Ultrahigh photooxidation performance

ABSTRACT

Low light-absorption capacity and separation efficiency of photo-generated charges are two major limit factors to achieve high performance of photocatalysts. Herein, porous core-shell $Ti_xSn_{1-x}O_2$ solid solutions with effective light-absorption capacity and charge separation are fabricated through one-pot mild solvothermal method without any surfactant and template. The self-development mechanism of the porous core-shell microspheres includes prior Ti -alkoxide hydrolysis and the spontaneous nucleation of $Ti_xSn_{1-x}O_2$ combined with Ostwald ripening. Interestingly, although both TiO_2 and SnO_2 are wide band gap semiconductors, the prepared yellow $Ti_xSn_{1-x}O_2$ solid solutions are of controllable band structure and broad-light response capacity. When $Ti:Sn$ molar ratio is 7:3, the $Ti_{0.7}Sn_{0.3}O_2$ sample shows the highest MO-photodegradation rate constant of 0.62 min^{-1} under UV irradiation, exceeding that of commercial TiO_2 (0.04 min^{-1}) by more than 15 times. Particularly, the sample also exhibits ultrahigh photocatalytic activity in MO-photodegradation (0.038 min^{-1}) and As(III) removal (up to 100%) under visible-light ($\geq 420\text{ nm}$) irradiation. The mechanism study reveals that due to the proper redox potential of Sn^{IV}/Sn^{II} and the structural defects (e.g., oxygen vacancies) caused by lattice distortion, the photo-generated electrons would be trapped and the holes act as the main active species for the photooxidation reaction of MO and As(III) over $Ti_xSn_{1-x}O_2$ photocatalysts.

1. Introduction

The global crisis of energy and environment pollution caused by the rapid growth of the population and industrial activities have increasingly received attentions. Efficient harvest, store and conversion of the freely available solar energy to solve the environmental and energy problems have become one of the hotspots of the current global researches. Since the first report on TiO_2 photocatalysis in 1972 [1], the semiconductors as photocatalysts has been proven to be a “green” and promising route for environmental remediation under solar irradiation [2–7]. Although TiO_2 has proven to be the most suitable for environmental applications, the performance of TiO_2 requires further enhancement due to the narrow light response range and low quantum efficiencies [8–10].

In comparison to the individual metal oxide, mixed metal oxides are more interesting which provides a controllable way to tailor the properties of materials over a broad range [11–14]. As suggested by Zakrzewska [15], the mixed metal oxide systems can generally be classified into three categories: (i) distinct chemical compounds, (ii) solid

solutions, and (iii) oxide composites (neither new compounds nor solid solutions). To date, considerable efforts have been devoted to develop the semiconductor solid solutions which band gap structure and redox potentials can be flexibly regulated by the relative proportion adjusting of the compounds. Many semiconductor solid solutions, such as SnO_2 - TiO_2 [16,17], $GaN-ZnO$ [18], $Ga_2O_3-In_2O_3$ [19], $ZnS-CdS$ [20,21], $BiVO_4-YVO_4$ [22], have been successfully prepared. The results show that the photoelectricity and catalytic properties are directly dependent on the compositions of materials.

Solid solutions of semiconductors TiO_2 and SnO_2 with wide band gap, denoted as $Ti_xSn_{1-x}O_2$ hereafter, are of great technological value. For example, doping Ti^{4+} can improve the sensing selectivity and stability of SnO_2 gas sensor [23], whereas Sn^{4+} additions in TiO_2 is an efficient way to enhance the photocatalytic activity [24]. Due to the very similar ionic radius of Ti^{4+} (0.68 \AA) and Sn^{4+} (0.71 \AA) and tetragonal crystal symmetry, complete miscible $Ti_xSn_{1-x}O_2$ solid solutions can be theoretically formed by the ion substitution. However, the metastable $Ti_xSn_{1-x}O_2$ ($0 < x < 1$) solid solutions can only be produced at elevated temperatures higher than the critical temperature [25],

* Corresponding authors.

E-mail addresses: jdzhuang@gmail.com (J. Zhuang), lihuichen66@126.com (L. Chen).

which depends on the molar ratio of TiO_2 to SnO_2 and reaches $\sim 1500^\circ\text{C}$ for 50 mol%. Moreover, only SnO_2 -rich ($x < 0.1$) and TiO_2 -rich ($x > 0.9$) solid solution phases are thermodynamically stable at room temperature [26]. Different preparation methods including sol-gel methods [27], chemical vapor deposition [28], co-precipitation [29], hydrothermal/solvothermal methods [30,31], mechanochemical synthesis [32], and electrospinning method [33] have been applied to synthesize $\text{Ti}_x\text{Sn}_{1-x}\text{O}_2$ materials for applications in gas sensors [34,35], heterogeneous catalysts [36,37], electrolyte materials [17,38]. The synthesis of $\text{Ti}_x\text{Sn}_{1-x}\text{O}_2$ solid solutions with full compositional range by facile one-step methods and low-cost raw materials have rarely been reported.

It is well known that the morphostructure can play an important role in the physiochemical performance of nanomaterials [39–44]. In recent years, inorganic porous, hollow and core-shell nanostructures have attracted extensive attentions due to the excellent diverse properties including low density, high surface area and good surface permeability [45–49]. For heterogeneous photocatalysis in particular, the high photocatalytic activity is strongly dependent on its specific surface areas and surface permeability [50–53]. Therefore, extensive studies have focused on controlling the hollow structure and morphology of metal oxide catalysts to achieve novel and enhanced properties. Numerous methods such as templating methods with either hard or soft templates [54–56], Kirkendall effect [39], Ostwald ripening [57,58], self-assembly techniques [59,60] have been widely employed in the wet fabrications. Among these, one-step and template-free hydro/solvothermal method based on Ostwald ripening has been proven to be a promising approach to generate interior space and shell porosity of inorganic microspheres [61,62]. For the preparation of thermodynamically metastable solid solutions, the direct synthesis of nanocrystals under hydro/solvo-thermal method would be worthy which high-temperature treatments for the crystallization are not required.

In present study, porous $\text{Ti}_x\text{Sn}_{1-x}\text{O}_2$ solid solution microspheres with a core-shell morphology is prepared by a facile one-pot and template-free solvothermal method. The experimental analyses highlighted that the physical Ostwald ripening process coupled with chemical conversion could induce the self-development of core-shell $\text{Ti}_x\text{Sn}_{1-x}\text{O}_2$ solid solution. The porous core-shell $\text{Ti}_x\text{Sn}_{1-x}\text{O}_2$ microspheres show improved performance for Methyl Orange (MO) and Arsenic (As(III)) oxidation-removal in aqueous solution. Explanations for the formation mechanism of core-shell $\text{Ti}_x\text{Sn}_{1-x}\text{O}_2$ microspheres and their excellent photocatalytic activities for organic dye and inorganic arsenic removal are also proposed.

2. Experimental

2.1. Catalyst preparation

Titanium-tin solid solutions $\text{Ti}_x\text{Sn}_{1-x}\text{O}_2$ (denoted as TSO-x, where $x = 0.9, 0.7, 0.5, 0.3$ or 0.1) are prepared by one-pot solvothermal method. All reagents are A.R. grade and used without further purification. In a typical synthesis, 1.5 mmol $\text{SnCl}_4 \cdot 5\text{H}_2\text{O}$ is dissolved in 70 mL ethanol under magnetic stirring to form clear solution. Subsequently 3.5 mmol titanium n-butoxide (TBOT) is added into the above solution with vigorous stirring, and the mixed liquid is stirred for an additional 15 min. The homogenous mixture is then sealed into a Teflon-lined autoclave, followed by solvothermal treatment at 180°C for 12 h. After cooled down naturally, the resulting $\text{Ti}_{0.7}\text{Sn}_{0.3}\text{O}_2$ solid product (denoted as TSO-0.7) is washed with deionized water and absolute ethanol for several times and dried at 60°C . A series of experiments with varying solvothermal temperatures and time are carried out to optimize the synthesis condition. Keeping the total molar amount (5 mmol) of TBOT and $\text{SnCl}_4 \cdot 5\text{H}_2\text{O}$ unchanged, TSO-x with varying Ti:Sn molar ratio are synthesized.

2.2. Photocatalyst characterizations

The as-prepared samples are characterized by powder X-ray diffraction (XRD) on a Bruker D8 Advance X-ray diffractometer at 40 kV and 40 mA with $\text{Cu K}\alpha$ radiation. A nitrogen sorption-desorption experiment is carried out at 77 K using an ASAP2020 surface area and porosity analyzer (Micrometrics Instrument). Field-emission scanning electron microscopy (FESEM) investigations are carried out on an FEI Nova NanoSEM 230 microscope. The structure is investigated by transmission electron microscopy (TEM) on a FEI Tecnai G2F20S-TWIN microscope. X-ray photoelectron spectroscopy (XPS) analysis is conducted on an ESCALAB 250 photoelectron spectrometer (Thermo Fisher Scientific). UV-vis diffuse reflectance spectra (UV-vis DRS) of the dry-pressed disk samples are obtained with a UV-vis spectrophotometer (Lambda750, PerkinElmer) using BaSO_4 as a reflectance standard. Raman spectra are collected using a HORIBA JY HR Evolution system (laser wavelength 532 nm) equipped with a $50 \times$ microscope objective lens under ambient conditions. A conventional three electrode cell using a ZENNium electrochemical workstation (Zahner, Germany) is used to determine the photoelectric properties of the sample. The catalyst sample is deposited on a 1 cm \times 1 cm ITO conducting glass served as working electrode, while the Ag/AgCl electrode as the reference electrode and Pt as the counter electrode. Electron spin resonance (ESR) spectra are obtained using Bruker model ESR 300E electron paramagnetic resonance spectrometer equipped with a quanta-Ray Nd:YAG laser system as the irradiation light source. The settings are center field, 3480.00 G; microwave frequency, 9.79 GHz; and power, 5.05 mW.

2.3. Photocatalytic degradation of MO dye

The photocatalytic degradation of MO dye in liquid phase was conducted in a quartz tube, which is illuminated by three surrounding wideband lamps (4 W, Philips TL/05) with a predominant wavelength at 365 nm. In a typical experiment, 80 mg photocatalyst is suspended in the quartz tube which contains 80 mL 10 ppm MO dye solution. Prior to irradiation, the solution was magnetically stirred in the dark for 30 min to ensure the establishment of an adsorption/desorption equilibrium between the photocatalyst and MO dye. At the given irradiation time intervals, 2 mL of the suspension is collected and centrifuged to obtain the upper clear solution, and analyzed on a UV-vis spectrophotometer (UV-6300, MAPADA). The change of MO absorbance in the solution was used to monitor the extent of reaction at given irradiation time intervals.

2.4. Photoinduced As(III) removal

Stock solution (1 g/L) of arsenite [As(III)] was prepared by dissolving 1.734 g of NaAsO_2 into 1 L 20% HCl solution. The reaction solutions (2 mg/L AsO_2^-) used for the As(III) removal experiments were made by diluting the stock solution and adjusting the pH value to the neutral state (~ 7.0) using 1 mol/L NaOH. In a typical As(III) removal experiment, 80 mg of TSO-x sample is suspended in a quartz tube which contained 80 mL dilute arsenic solution (2 mg/L AsO_2^-). The suspension is stirred magnetically and illuminated by a 150 W tungsten-halogen lamp (LSH-T150, ZOLIX) with two glass filters (420–800 nm). For comparison, an As(III) photolysis process without catalysts was also performed under the same conditions. At the given irradiation time intervals, 1 mL of the suspension was collected, and then centrifuged to remove the photocatalyst. After recovering the photocatalyst by centrifugation, the pH value of the arsenic solution were adjusted to 4 through the dripping of concentrated HCl. Atomic fluorescence spectrometry (PF6, Beijing purkinje general instrument co.,ltd.) was used to analyze the As(III) content in the reaction solution. And the used photocatalyst was analyzed by XPS to indicate the chemical states of As after the photocatalytic reaction.

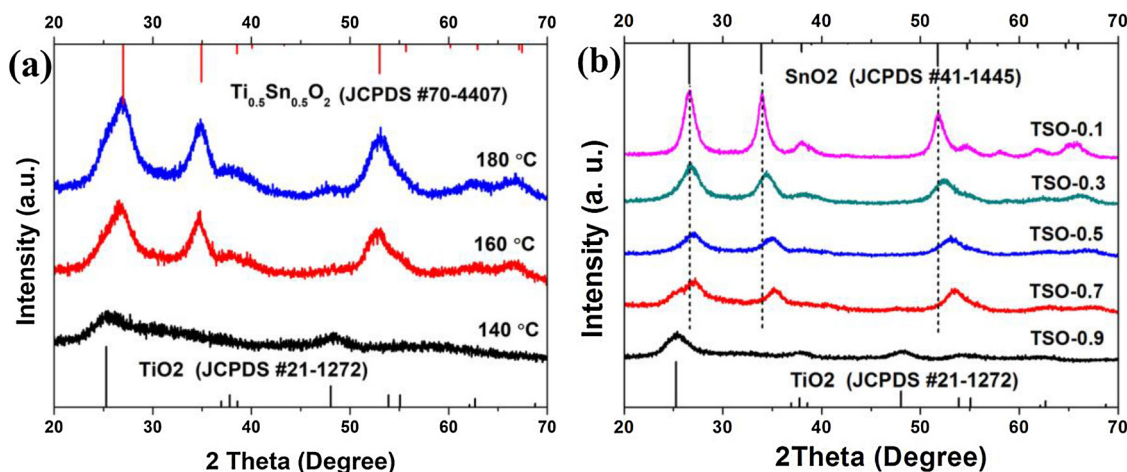


Fig. 1. XRD patterns of (a) TSO-0.5 samples prepared at different temperatures for 12 h, and (b) TSO-x solid solution samples with varying x prepared at 180 °C for 12 h.

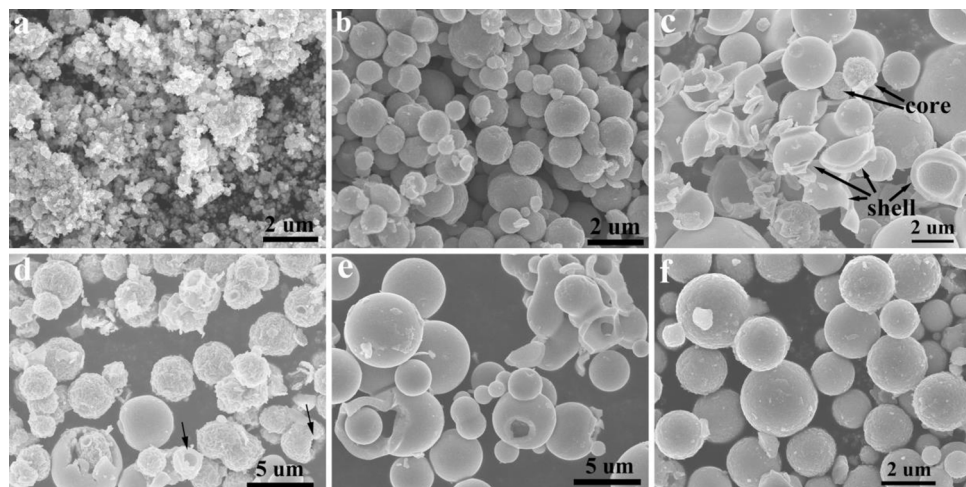


Fig. 2. SEM images of TSO-x solid solution samples with varying x prepared at 180 °C for 12 h, (a) SnO_2 , (b) TSO-0.1, (c) TSO-0.3, (d) TSO-0.5, (e) TSO-0.7, and (f) TSO-0.9.

3. Results and discussion

3.1. Phase and morphology analyses of TSO samples

The phase and purity of TSO-x nanoparticles are determined by powder XRD technique, and the indexed powder XRD patterns are shown in Fig. 1. It is obvious that the synthetic temperature plays an important role in controlling crystal phases and sizes of the final products. Fig. 1a shows XRD patterns for TSO-0.5 synthesized at different temperatures for 12 h. At relative lower temperature 140 °C, the product shows broaden and weak diffraction peaks which could possibly be indexed to anatase TiO_2 (JCPDS #21-1272). When the synthetic temperature is higher than 160 °C, the diffraction peaks become sharper. For the sample prepared at 180 °C, all the diffraction peaks matched well with the characteristic reflections of $\text{Ti}_{0.5}\text{Sn}_{0.5}\text{O}_2$ (JCPDS #70-4407). The peaks at 2θ values of 27.0°, 34.9°, 38.6°, and 53.0° can be corresponded to (110), (101), (200), and (211) crystal planes of $\text{Ti}_{0.5}\text{Sn}_{0.5}\text{O}_2$ with tetragonal structure. The broaden diffraction peaks of TSO-0.5 indicate a primary crystallite size of approximate 4.0 nm, calculated from Debye-Scherrer equation based on the main diffraction peak (110). The overfine crystal size of the solid solution is probably due to a distortion in the lattice caused by the discrepancy in the ionic radius of Sn^{4+} ion (71 pm) and Ti^{4+} ion (68 pm). The existence of Ti-O-Sn in the solid solution can also inhibit the growth of crystal grains by providing

dissimilar boundaries. [24,27]

Fig. 1b displays XRD patterns for TSO-x with varying x, and the diffraction peaks of crystalline phases are compared with the standard JCPDS pattern of pure anatase TiO_2 and cassiterite SnO_2 . TSO-0.9 with high Ti amount mainly consists of anatase TiO_2 phase. With increasing Sn molar ration, phase transition is observed, which is further proved by the Raman spectra (Fig. S1) and also witnessed as the diffraction peaks of nanoparticles are shifted to higher 2θ values. The qualitative XRD analysis reveals that the positions of diffraction peaks closely match with the standard values known for the respective solid solution systems (JCPDS #70-4405 ~ #70-4411). No phases of other oxides, impurities or separate nucleation of Ti/Sn/O has occurred, strongly suggesting that the Ti atoms can be substituted by the intervening Sn atoms to form the stoichiometric Ti-Sn solid solution under the mild solvothermal method. By further reducing Ti molar amount to zero, the final product turns out to be pure cassiterite SnO_2 phase. Furthermore, it is hard to produce TiO_2 under the same synthesis conditions without addition of $\text{SnCl}_4 \cdot 5\text{H}_2\text{O}$, implying that the crystal water in $\text{SnCl}_4 \cdot 5\text{H}_2\text{O}$ plays an important role in the formation of the titania crystallite. The structural parameters of $\text{Ti}_x\text{Sn}_{1-x}\text{O}_2$ nanocrystals are calculated and summarized in Table S1.

Morphologies analysis of TSO-x solid solutions are performed by FESEM (Fig. 2). These micrographs depict that the morphology, particle size, as well as the aggregate status of the TSO solid solution

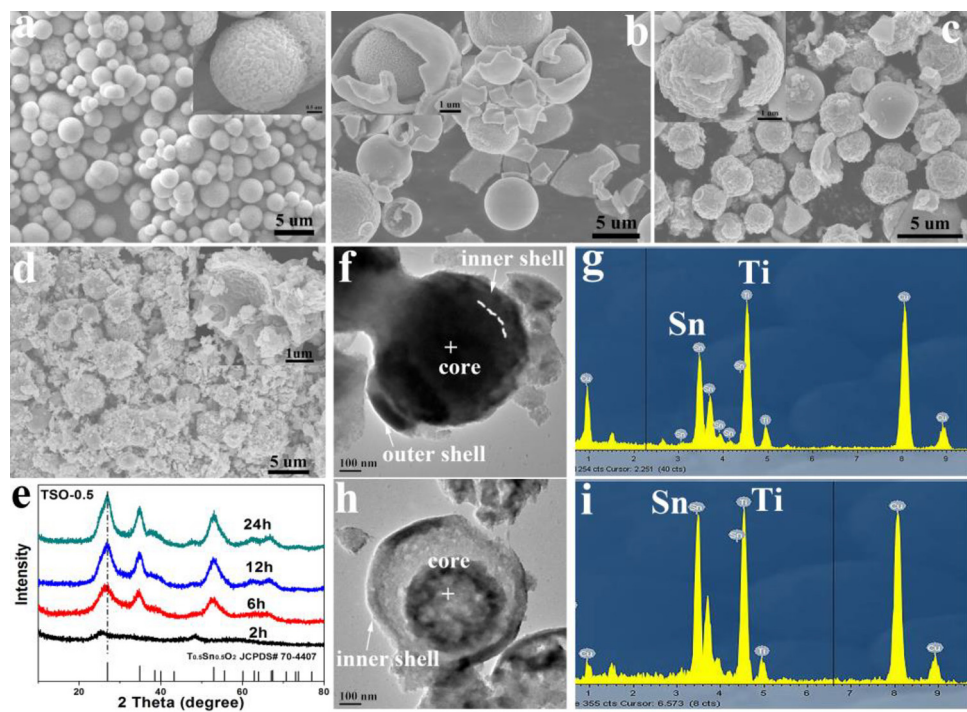


Fig. 3. SEM images (a–d), XRD patterns (e), TEM images (f, h) and corresponding EDS spectra (g, i) of TSO-0.5 samples obtained after different processing times. (a) 2 h, (b, f, g) 6 h, (c, h, i) 12 h, and (d) 24 h. Insets show the partial enlarged detail of samples.

significantly vary with Ti:Sn ratios. A large number of irregular SnO_2 particles with small size are uniformly generated by only using $\text{SnCl}_4 \cdot 5\text{H}_2\text{O}$ as precursor (Fig. 2a). When TBOT is added, the TSO-0.1 appears as solid microsphere with uneven particle size (Fig. 2b). Increasing the Ti:Sn ratio to 3:7, the enlarged microspheres can be clearly seen in Fig. 2c, which the broken spheres reveal that the particles is composed of porous spherical core and relatively condense shell. For TSO-0.5, with the increase of Ti content, the porous core spheres further grow up to approximately 2–3 μm , and tend to detach from the outside shell (Fig. 2d). It is interesting to note that the core microspheres also possess hollow interiors structure, as indicated with arrows in the figure. For TSO-0.7, microspheres with core-shell structure can also be clearly observed (Fig. 2e), and some spheres are connected to each other, forming a grape-like structure. Further increase the Ti:Sn ratio to 9:1 (TSO-0.9), the particles turn back to be solid microsphere (Fig. 3f). In brief, the results indicate that when the Ti-Sn contents are closed to each other, products with morphologies of porous core-shell microspheres can be formed readily.

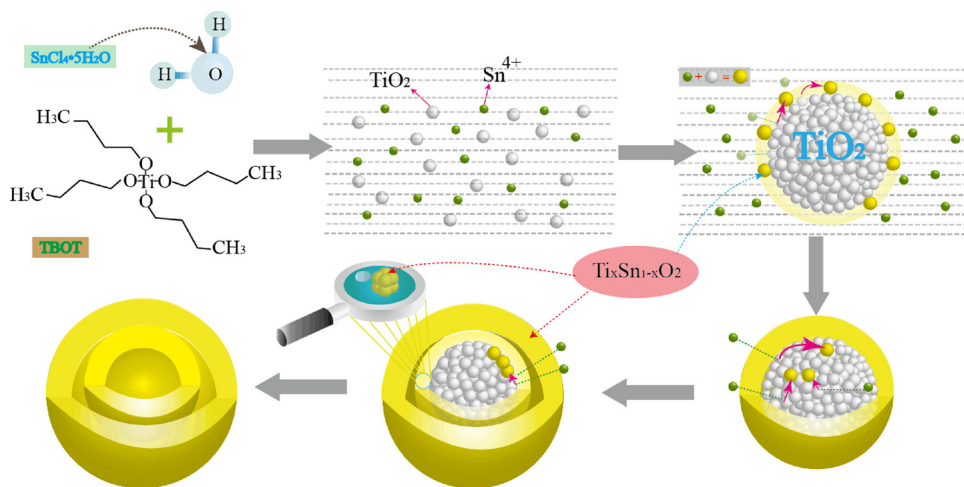
To illustrate the formation mechanism of the core-shell TSO-0.5 solid solution nanostructures, an investigation using SEM and XRD is conducted to monitor the time-dependent morphological evolution and crystallization process. Fig. 3a–d show the FESEM images of TSO-0.5 at 180 °C for varying solvothermal treatment times. The microspheres with solid core structure are initially formed after 2 h of solvothermal reaction (Fig. 3a). The corresponding XRD pattern (Fig. 3e) exhibits that the product is poor crystalline, but the diffraction peaks still able be ascribed to anatase TiO_2 phase. It should be noted that some microspheres are of a rough surface (inset of Fig. 3a), implying the etching (restructure) reaction takes place on the TiO_2 microspheres during the synthesis process. The restructure as well as crystallization phenomena continue with the solvothermal reaction time prolonging. As shown in Fig. 3b and inset, the product obtained at 6 h appears as core-shell microspheres (porous core and solid shell), and its XRD pattern can be exclusively indexed to $\text{T}_{0.5}\text{Sn}_{0.5}\text{O}_2$ solid solution (JCPDS#70-4407). The core-shell microstructure can be confirmed by the TEM image (Fig. 3f). A contrast between the relative bright margin and black center observed in the core further indicates the dynamic process of

hollowing. When time prolongs to 12 h, the porous TSO core-shell nanostructures can fully be developed (Fig. 3h). Such porous core-shell structure is critical for catalysts since it can provide tremendous transport pathways to interior voids. The SEM image (Fig. 3c) also confirms the formation of mainly porous microspheres which are detached from the outside shell. Interestingly, the wormlike shell of the core spheres looks different from those of Fig. 3h, and the cracked sphere (inset of Fig. 3c) reveals the core spheres possess core-shell structure as well. Further prolong solvothermal time to 24 h (Fig. 3d), a great amount of TSO solid solution fragments can be observed. The XRD peaks become sharper with processing time (Fig. 3e), with no extra diffraction peaks, indicating no spinodal decomposition of TSO solid solution occurs during the synthesis process.

To determine the chemical conversion of the core-shell particles, energy-dispersive X-ray spectroscopy (EDS) analysis coupled TEM microscope is used to examine the elements in each individual micro-particle. The test region is selected near the center of a single microsphere, and the results of the TSO-0.5 at 6 h and 12 h processing time are shown in Fig. 3g and i, respectively. Both spectra are dominated by Sn and Ti signals accompanying some Cu peaks (arise from the mesh copper grids). For the TSO-0.5 at 6 h, the atom ratio of Ti:Sn is approximately 10:7 (Fig. 3g), revealing the core sphere is rich of Ti element (TiO_2 core). With the processing time prolonging, the hollowing process in the central section would continue to form the hollow core-shell stoichiometric Ti-Sn solid solution by draining inner Ti(OH)_4 core (Fig. 3i). The restructure phenomena are based on Ostwald ripening which involved with chemical conversion and solid-solution-solid transformation.

3.2. Tentative mechanism for the formation of multiple core-shell TSO microspheres

We proposed that multiple core-shell TSO solid solution microspheres are formed via Ostwald ripening by using a simple one-pot solvothermal method (Scheme 1). Hydrolysis is initiated between $\text{Ti}(\text{C}_4\text{H}_9\text{O})_4$ and the crystal water of $\text{SnCl}_4 \cdot 5\text{H}_2\text{O}$ to form Ti(OH)_4 hydrogel grains with poor crystallinity. To minimize the surface energy, the small



Scheme 1. Schematic illustration of the process to prepare core-shell TSO-x solid solutions.

hydrogel grains would assemble together as solid spheres. The poorly crystallized $\text{Ti}(\text{OH})_4$ are more active than pure TiO_2 , while incorporation of Sn^{4+} leads to metastable heterogeneous nucleation of $\text{Ti}_x\text{Sn}_{1-x}\text{O}_2$ at appropriate solvothermal temperature. In the spontaneous nucleation process, the chemical conversions of Ti-based hydrogel could shrink the grains and cause voids inside the hydrogel spheres. Additionally, Due to the insufficient rapid nucleation poor crystallinity of the $\text{Ti}_x\text{Sn}_{1-x}\text{O}_2$ nucleus cause the redissolution and relocation dictated by Ostwald ripening upon further reactions. Considering the solubility of nucleus at the relatively high solvothermal temperature, the inner crystal nucleus would dissolve to minimize the surface energy, and migrate outward to the surface to form larger recrystallized particles. During the growth process, these particles around the outmost surface become compact, leading to the formation of core-shell (porous core and solid surface shell) microspheres. Since the solid shells tend to break up in the process of centrifugation, the shell fragments and the detached porous core particles could be observed in the SEM images.

It should be mentioned that the chemical reaction and spontaneous nucleation of Ti-Sn ions is relatively slow and insufficient, there are still residues of $\text{Ti}(\text{OH})_4$ in the core particles after the formation of primary core-shell microspheres. Therefore, the spontaneous nucleation and Ostwald ripening are continuous. At the expense of the residual Ti-based hydrogel inside, the crystallites on the exterior surface of core microspheres further grow via Ostwald ripening to form new core-shell microspheres [58]. Moreover, drain off the inner grains would result in a cavity space inside the spherical core particles. With the complete chemical conversion of Ti-based materials, the core-shell microsphere with hollow core would finally be well developed. The core-shell structure of TSO solid solutions could allow the entrance and multiple reflection of light in the interior cavity, leading to more efficient absorption of the light [51].

3.3. UV-vis diffuse reflection spectra and band structure analyses

The photo-response performance is an important index of the photocatalysts. In particular, although both SnO_2 and TiO_2 are wide band gap semiconductors with white color, TSO solid solution are yellow. Such phenomena are also observed in the $(\text{Ga}_{1-x}\text{Zn}_x)(\text{N}_{1-x}\text{O}_x)$ solid solution [18]. The optical absorptions of $\text{Ti}_x\text{Sn}_{1-x}\text{O}_2$ ($x = 0, 0.1, 0.3, 0.5, 0.7$, and 0.9) are characterized with UV-vis diffuse reflection spectra (DRS), and the obtained spectra and corresponding colors are compared in Fig. 4a. Obviously, the absorption edges of $\text{Ti}_x\text{Sn}_{1-x}\text{O}_2$ solid solutions shows a continuous red-shift with increasing Ti:Sn ratio, confirming the formation of not simple mixtures but solid solutions. The corresponding color changes from white (SnO_2 , not shown), pale yellow to bright orange can also be observed in the inset of Fig. 4a. Additionally, the

continuous changes in the absorption edges and colors also reveals the band gaps of the $\text{Ti}_x\text{Sn}_{1-x}\text{O}_2$ solid solutions can be regulated by control the molar ratios of Ti and Sn precursors. The direct band gaps of the TSO solid solution can be determined by tangent of the Kubelka-Munk (K-M) curve at the onset region. As listed in Table 1, the band gaps decrease from 3.522 eV (SnO_2) to 2.701 eV (TSO-0.9) with the increasing x value from 0 to 0.9, indicating that substitution of the cations would narrow the band gap for more photons absorption and possibly yield the visible-light photoactivity.

Nevertheless, there is still controversy about the effects of substitutional Sn on the optical absorption changes of the TSO-x solid solution. The substitution of Sn for Ti leads to a blue-shift of the optical absorption edge of TiO_2 [24,63,64]. Sn-doping can extend the optical absorption of TiO_2 to visible-light region [36,65–68]. Harunsani et al. [66] prepared a dilute solid solution $\text{Sn}_x\text{Ti}_{1-x}\text{O}_2$ ($0.0 < x < 0.1$) which Sn doping lead to narrowing of TiO_2 band gap with a minimum of 2.95 eV. They attributed such behavior to the appearance of new states (the segregated Sn(II) cations occupying) above valence band minima of TiO_2 . We attribute two main reasons for the broad-light response of the TSO-x solid solutions. Firstly, when Sn^{4+} is substituted by Ti^{4+} , TSO solid solution should exist in a strained form due to the size difference between Sn^{4+} (0.71 Å) and Ti^{4+} (0.68 Å). [63] To offset the lattice strain, the structural defects such as oxygen vacancies (V_O) would be generated and cause the changes in surface states, electric structure and optical properties of oxide. [65,66,69] Secondly, substitution of Sn^{4+} for Ti^{4+} leads to the shift of the band edge. Although the Ti 3d states dominate the low portion of the conduction band, some gap states (mostly composed of the Sn 5s orbitals) can mix and lower the conduction band edge of TSO-x solid solutions, [70] leading to red-shift of the absorption edge.

Besides the band gap width, the band gap edge position is also important for effective photo-redox activity of semiconductor photocatalysts. The conduction band (CB) edge positions of the prepared TSO samples can be determined by the following equation:

$$E_{\text{CB}} = X - E^{\text{c}} - \frac{1}{2}E_{\text{g}} \quad (1)$$

$$X = (x_{\text{Ti}}^x \times x_{\text{Sn}}^y \times x_{\text{O}}^z)^{1/(x+y+z)} \quad (2)$$

$$x = \frac{1}{2}(A + I) \quad (3)$$

where E_{CB} is the conduction band edge potential. X is the absolute electronegativity of the semiconductor (Eq. (1)), expressed as the geometric mean of the absolute electronegativity (x) of the constituent atoms (Eq. (2)). The absolute electronegativity of an individual atom is the arithmetic mean of the atomic electron affinity (A) and the first

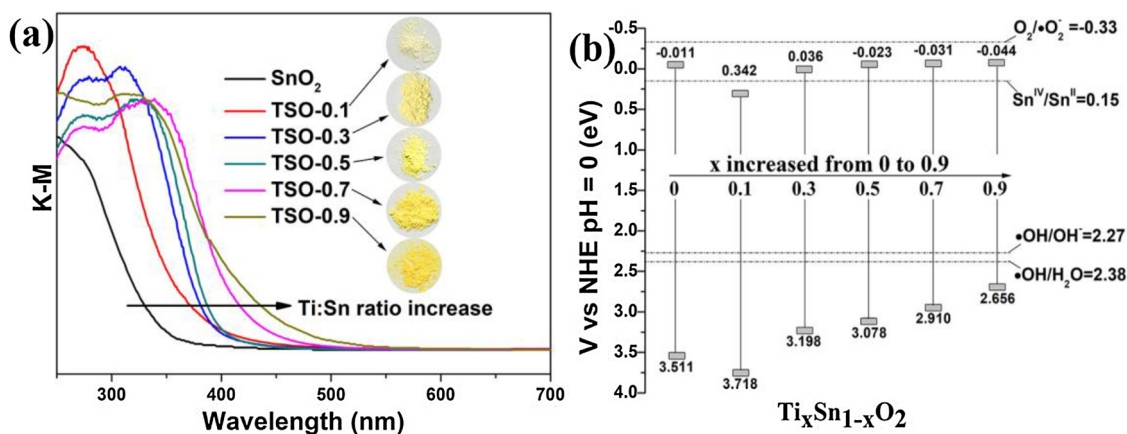


Fig. 4. (a) UV-vis diffuse reflection spectra, and (b) the calculated band gap edge potential of the $\text{Ti}_x\text{Sn}_{1-x}\text{O}_2$ ($x = 0, 0.1, 0.3, 0.5, 0.7$ and 0.9) samples.

Table 1

Crystallite size, BET specific surface area (S_{BET}), pore size, band gap energy and MO degradation rate constants of the TSO-x samples.

| x | Crystallite Size [nm] ^a | S_{BET} [m ² /g] | Pore size [nm] | Band gap [eV] | MO Degradation Rate Constants [min ⁻¹] | |
|-----|---------------------------------------|---|-------------------|------------------|---|---------------|
| | | | | | UV | Visible-light |
| 0 | 6.6 | 89.4 | 3.73 | 3.522 | 0.003 | – |
| 0.1 | 5.8 | 113.2 | 3.55 | 3.376 | 0.13 | 0.004 |
| 0.3 | 4.3 | 150.1 | 3.58 | 3.162 | 0.07 | 0.010 |
| 0.5 | 4.0 | 220.2 | 3.64 | 3.101 | 0.15 | 0.014 |
| 0.7 | 3.7 | 192.5 | 3.92 | 2.941 | 0.62 | 0.038 |
| 0.9 | 3.5 | 126.6 | 4.83 | 2.701 | 0.34 | 0.032 |

^a Determined by the FWHM of (110) facet diffraction peak using Scherrer equation.

ionization energy (I) (Eq. (3)). The absolute electronegativity value of Ti, Sn, and O is reported to be 3.45, 4.30, and 7.54, respectively [71]. E^c is the energy of free electrons on the hydrogen scale (~ 4.5 eV). E_g is the direct band gap of the semiconductor.

The band gap edge potential of TSO solid solutions are illustrated in Fig. 4b. Compared with the band gap edge of pure SnO₂ and TiO₂ (not shown), remarkable changes can be observed in both CB and VB edge potentials of TSO-x, indicating the cations substitution would seriously change the band gap structure of pure SnO₂ or TiO₂. A small amount of Sn substitution leads to narrowing of TiO₂ band gap with a minimum of 2.701 eV (Fig. 4b). With increasing Sn content, the Sn_xTi_{1-x}O₂ showed a monotonic increase in the direct band gap, which agrees well with the periodic DFT calculation by Sensato et al. [64]. A slightly lower shift in the conduction band position of TSO-x can be observed at the same time, confirming the hybridization between Sn 5s and Ti 3d orbitals. The shift of the band gap edge implies the redox ability can be regulated by controlling the Ti:Sn molar ratios. A balance between the light absorption capacity and the redox power in the TSO-x solid solution can lead to different photocatalytic efficiencies under irradiations.

3.4. Chemical environment and N₂ adsorption/desorption analyses

XPS analysis is explored to gain deeper insight to the chemical and bonding environments of the prepared TSO-x solid solutions, and surface composition change at Ti:Sn molar ratios. All binding energies are referenced to the C 1s neutral carbon peak, which is assigned the value of 284.6 eV to compensate for surface charge effects. Fig. 5 shows the Sn 3d and O 1s regions of the XPS spectra for TSO-x solid solutions. In agreement with previous studies of SnO₂ [72], the binding energy of Sn 3d_{5/2} core line of pure SnO₂ sample is observed at ~ 486.4 eV (Fig. 5a), indicating that tin element mainly existed as Sn⁴⁺. Note that the Sn 3d

peaks show two types of spectral changes with the increase of Ti⁴⁺ addition: one is the lower-shift in binding energy of Sn 3d line, the other is the decline in the peak intensity. These spectral changes prove that the Sn is substituted by the Ti, and the Sn ions would exist with lower valence due to the existence of oxygen vacancies.

The existence of oxygen vacancies might also lead to the surface chemisorbed oxygen groups. As shown in the Fig. 5b, there is a shoulder located at the high binding energy side of the main O 1s peak of TSO-x ($x = 0.3, 0.5, 0.7$), indicating the coexistence of different oxygen chemical states. The peaks at ~ 531.5 eV and ~ 532.8 eV can be attributed to the chemisorbed hydroxyl groups ($-\text{OH}$) and C–O bonds, respectively. [52] As compared with TSO-0.3, the TSO-0.5 and TSO-0.7 samples possess a strengthened $-\text{OH}$ peak, implying a higher amount of chemisorbed hydroxyl groups. The chemisorbed oxygen groups are mainly dependent on the surface defects (oxygen vacancies, V_{O}) present on the surface of TSO solid solution. Moreover, the surface hydroxyl groups could play an important role in photocatalytic activity, which interact with holes generated by UV illumination to form hydroxyl radicals and prevent electron-hole recombination.

The oxygen vacancies of the TSO-x ($x = 0.3, 0.5, 0.7$) samples are further examined by the powder electron spin resonance (ESR) technique. ESR is a common and powerful tool to determine the unpaired electron species (e.g., free radicals or V_{O}^{\cdot}). [52,74,75] Fig. 6 displays the ESR spectra of TSO-x samples measured at room temperature without irradiation. It can be observed that for all three samples, there is a symmetrical ESR signal attributable to the electron traps on oxygen vacancies (V_{O}^{\cdot}) located at $g = 2.002$ (~ 3508 Guass). No other (e.g., Ti³⁺) ESR signal was detected under the same test condition. The ESR results demonstrated that highly stable V_{O} defects can be formed in the TSO solid solution. Note that the intensities of the ESR signals differ obviously and show in the descending order of TSO-0.5 > TSO-0.7 > TSO-0.3.

Fig. 7 shows the pore size distribution curves and N₂ adsorption-desorption isotherms (inset) of Ti_xSn_{1-x}O₂ samples ($x = 0.3, 0.5$ and 0.7). The nitrogen isotherms are of type IV (Brunauer-Deming-Deming-Teller classification) and have a hysteresis loop (type H₂) in the relative pressure range of 0.4–0.8, indicating the presence of ink-bottle mesopores (2–50 nm, inset in Fig. 7) formed between intra-agglomerated nanoparticles. The isotherm of sample TSO-0.5 shows an increased adsorption in high P/P_0 range ($0.8 < P/P_0 < 1.0$), suggesting the formation of macropores. The quantitative details on the BET surface areas (S_{BET}) and average pore sizes of the as-prepared Ti_xSn_{1-x}O₂ samples ($0 \leq x \leq 1$) are summarized in Table 1. All three core-shell TSO-0.3, 0.5 and 0.7 solid solutions exhibit large specific surface areas, which is contributed to the unique nanostructure.

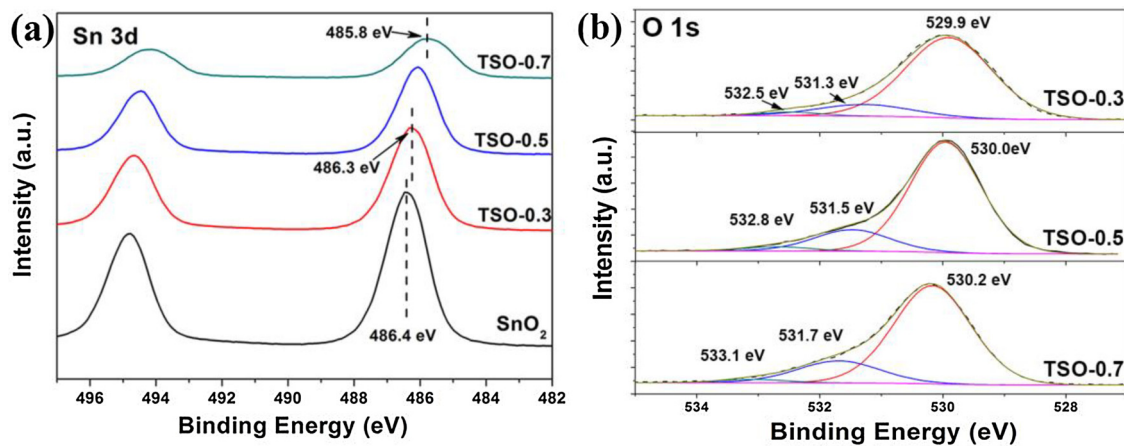
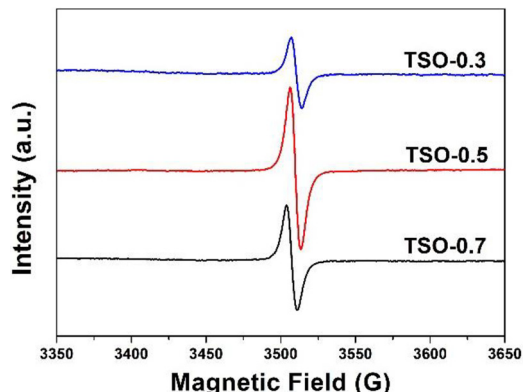
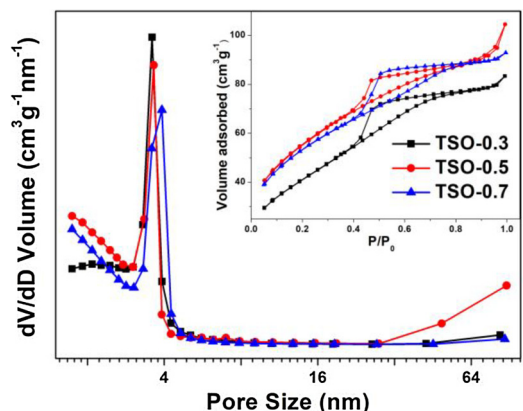


Fig. 5. Sn 3d (a) and O 1s (b) XPS spectra of the TSO-x solid solutions.

Fig. 6. Room temperature ESR spectra of the TSO-x ($x = 0.3, 0.5, 0.7$) samples.Fig. 7. Pore size distribution curve and N_2 adsorption-desorption isotherms (inset) of TSO-x ($x = 0.3, 0.5, 0.7$) samples.

3.5. Photocatalytic activity analyses

For photocatalyst, generally, large specific surface area, suitable band gap edge potential and band gap width attribute to the optimal photocatalytic activity under irradiation. The photocatalytic activities of TSO-x are evaluated by the degradation of Methyl Orange (MO) under UV (365 nm) or Visible light ($420 \leq \lambda \leq 800$ nm) irradiation. The temporal changes in the concentration of MO over photocatalysts under different experimental conditions are shown in Fig. 8. The concentration of MO exhibited almost no change without photocatalysts (Fig. 8a), indicating it is stable under UV irradiation. With TSO photocatalysts and UV irradiation, the concentration of MO decline rapidly,

meaning all the TSO solid solutions are promising photocatalysts for dye degradation (Fig. S3). The photocatalytic activities of TSO for MO degradation are in the descending order of TSO-0.7 > TSO-0.5 > TSO-0.3. TSO-0.7 possesses a remarkable photocatalytic activity for MO degradation, with the degradation ratio up to 91.5% after 4 min UV irradiation. The corresponding MO degradation rate constant of TSO-0.7 is calculated to be 0.62 min^{-1} , exceeding that of pure TiO_2 (P25, 0.04 min^{-1}) by more than 15 times. In order to evaluate the photostability of the solid solutions, the cyclic photodegradation of MO over TSO-0.7 sample is also conducted under UV irradiation (SI-4). As shown in Fig. S3, the TSO-0.7 solid solution exhibits a good photostability with trivial loss of photocatalytic activity toward the degradation of MO after three cycles.

As expected, under visible-light ($420 \leq \lambda \leq 800$ nm) irradiation, all three TSO solid solutions show excellent photocatalytic activity for MO degradation (Fig. 8b). For TSO-0.7, the degradation efficiency to MO can reach approximately 94% after 60 min visible light irradiation. Similar photoactivity descending order of TSO-0.7 > TSO-0.5 > TSO-0.3 can be observed under the condition of visible light excitation. After taking the specific surface area into consideration, the degradation rates per unit area of the samples still follow the same order. Thus, the change in surface area of TSO solid solutions is not a crucial factor leading to greatly improved photoactivity. Typically, TiO_2 and SnO_2 cannot absorb visible light due to the large band gap width ($> 3.0 \text{ eV}$). For TSO solid solution, the balance among the factors of energy band position, light-absorption capacity, and surface absorbed hydroxyl groups contribute to the high photocatalytic performance. Based on the results of powder ESR and photocatalytic activity tests, it is deduced that the photoactivity of TSO is close related with the oxygen vacancies. A suitable concentration of defective sites can act as shallow traps for electrons and thus enhances the carriers separation, thus the photocatalytic activity of TSO-0.7 is higher than that of the TSO-0.3 samples. While for the TSO-0.5, the excessive V_O defects will suppress the charge transfer efficiency of the photocatalyst, therefore, the TSO-0.5 sample shows a lower activity than TSO-0.7 sample. The results prove that the oxygen vacancies would play a predominant role in photocatalytic activity of TSO solid solutions.

To further elucidate the primary active species such as $\cdot OH$, $\cdot O_2^-$ and photogenerated hole (h_{VB}^+) involved, the effects of radical scavengers and nitrogen on the photocatalytic degradation efficiency of MO are investigated. The inhibition effects of scavengers on MO degradation are in the descending order of ammonium oxalate (h_{VB}^+ scavenger) > isopropanol ($\cdot OH$ scavenger) > N_2 (O_2 scavenger), implying the h_{VB}^+ and $\cdot OH$ radicals play predominant roles in the photocatalytic process (Fig. 9a). The efficient anoxic degradation of MO further confirms the superoxide radical ($\cdot O_2^-$) is inactive for the dye photodegradation of MO/TSO-x system.

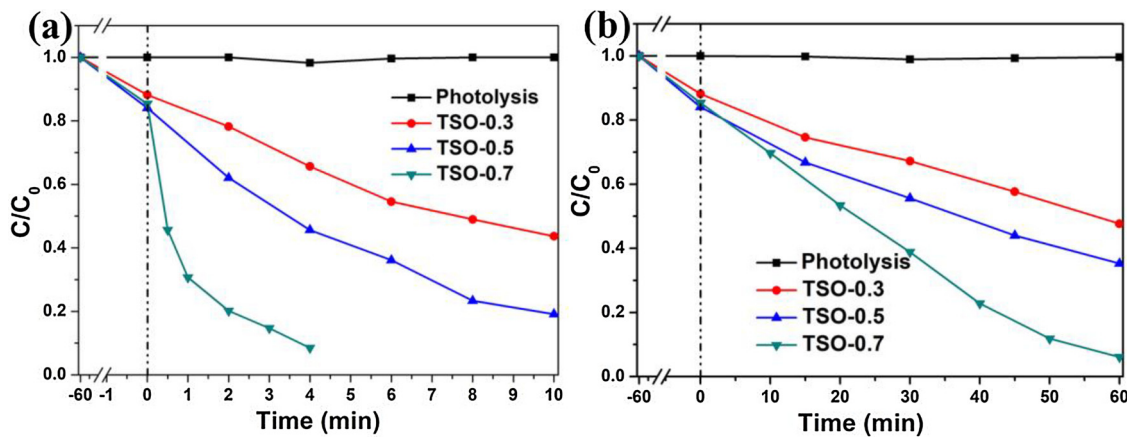


Fig. 8. Photocatalytic performances of TSO-x ($x = 0.3, 0.5, 0.7$) for degradation 10 ppm MO under (a) UV 365 nm and (b) Visible light ($420 \leq \lambda \leq 800$ nm), respectively.

On the basis of the above band structure analysis (Fig. 4b), it is found that the valence band potentials (E_{VB}) of all TSO-x are much more positive than $E_0(\text{OH}/\text{H}_2\text{O})$ (2.38 V vs. NHE), while the conduction band potentials (E_{CB}) of the TSO samples are less negative than the $E_0(\text{O}_2/\text{O}_2^-)$ (-0.33 V vs. NHE) [76]. Therefore, for the irradiated photocatalysis system, the $\cdot\text{OH}$ radicals can theoretically formed from the h_{VB}^+ induced oxidation of hydroxyl groups, but the adsorbed O_2^- would not be reduced by excited electrons (e_{CB}) to generate $\cdot\text{O}_2^-$ radicals. This deduce can further be proved by the ESR spin-trap with DMPO technique. Under 365 nm irradiation, four characteristic peaks of DMPO- $\cdot\text{OH}$ can be obviously observed in the suspension of TSO-0.7, while only very weak peaks for the DMPO- $\cdot\text{O}_2^-$ species can be observed in TSO-0.7 methanolic dispersions (Fig. 9b). The result indicates that the photogenerated carriers in TSO solid solutions possess a good separation efficiency, and the excited holes (h_{VB}^+) are long-lived enough to react with surface adsorbed hydroxyl groups to form $\cdot\text{OH}$ radicals. Possibly three main reasons account for the high separation efficiency and the long-lived h_{VB}^+ . Firstly, as proposed by Sensato et al. [64] Sn substitution for Ti in TiO_2 can render the lowest energy transition between CB and VB to be forbidden, thus would prevent the recombination of photogenerated carriers effectively. Secondly, structural defects such as oxygen vacancies (V_O) would act as shallow traps for electrons and thus also enhance the electron-hole pair separation efficiency. [10,65] Thirdly, because the standard redox potentials for the $\text{Sn}^{IV}/\text{Sn}^{II}$ redox couples (0.15 V vs. NHE) is more positive than the E_{CB} of the TSO samples, the photogenerated e^- would reduce Sn^{4+} ions to lower valence and leads in consequence to a decrease in the recombination rate.

The oxidation of Arsenite (As(III)) to Arsenate (As(V)) is highly desirable because As(III) is much more toxic and less efficiently removed than As(V) [77,78]. Considering the high efficient photooxidation capability of TSO-x, we choose As(III) as a simulative pollutant to estimate the photooxidation performance of the TSO solid solution under visible light irradiation. The temporal changes of the As(III) concentration over TSO-0.7 under different experimental conditions are shown in Fig. 10a. Obviously, the As(III) is very stable for visible light irradiation. After 30 min of dark adsorption with TSO-0.7, the removal amount of As(III) is examined to be approximate 58%, suggesting the As(III) species can available adsorb on the TSO solid solution surface. The As(III) removal rate are remarkably accelerated with visible light irradiation. After 30 min irradiation, the atomic fluorescence signal of As(III) is undetectable in the suspension, confirming the TSO solid solution is of high efficiencies in As(III) adsorption and oxidation. XPS is further used to investigate the chemical states of the As species adsorbed on TSO-0.7 photocatalyst before and after the reaction. It can be seen in Fig. 10b that after photocatalytic reaction, the peak located at ~ 44.36 eV (assigned to As(III)) shift to higher binding energy side (~ 45.23 eV, assigned to As(V)), implying the effective photooxidation of As(III) to As(V) by TSO-0.7 solid solution. On the basis of above discussions, the TSO solid solutions, which show high performance in dye degradation and As(III) removal under either UV or visible light irradiation, are proposed to be promising photocatalysts for aquatic pollution remediation.

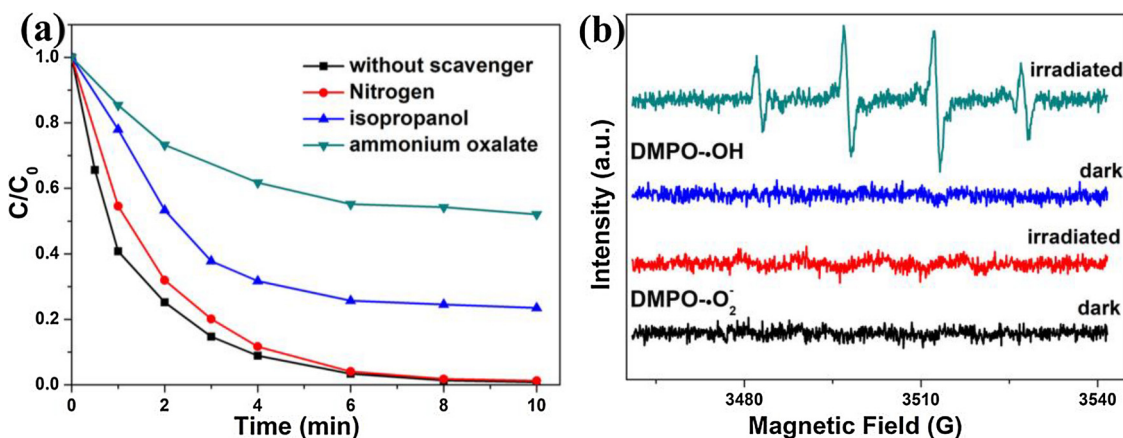


Fig. 9. (a) Photocatalytic performances of TSO-0.7 with radical scavengers. (b) DMPO spin-trapping ESR spectra of TSO-0.7 in aqueous dispersion for DMPO- $\cdot\text{OH}$ and in methanol dispersion for DMPO- $\cdot\text{O}_2^-$, respectively.

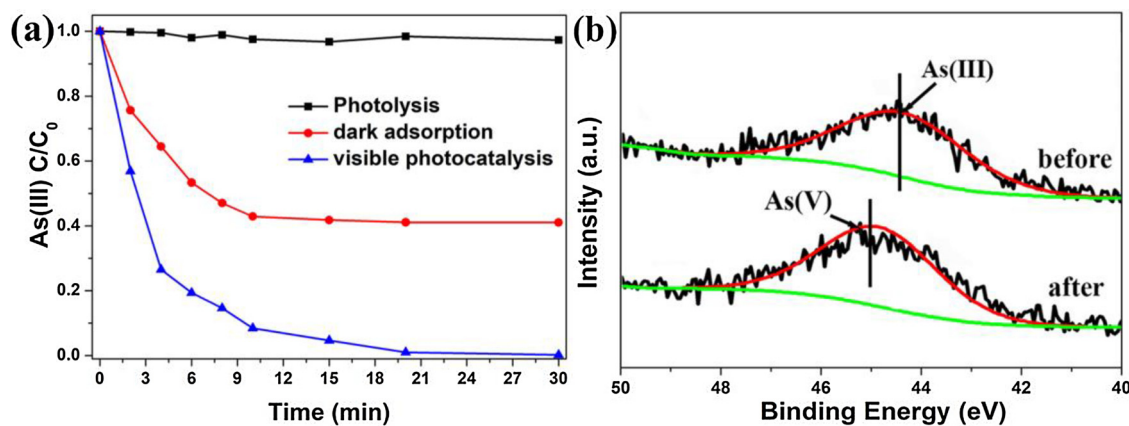


Fig. 10. (a) Temporal changes of the As(III) concentration over TSO-0.7 under different experimental conditions, and (b) As 3d XPS spectra of TSO-0.7 photocatalysts collected before and after irradiation.

3.6. Photoelectrochemical analyses

The formation and transfer of electrons are investigated by electrochemical analysis including chronoamperometry response and electrochemical impedance spectroscopy (EIS). Fig. 11a, b present the periodic photocurrent responses of representative photocatalysts including TSO-0.3, TSO-0.5 and TSO-0.7 under intermittent UV and visible light irradiation. Both UV and visible-light induced photocurrent (I_{ph}) of all samples at 0.2 V is constant with good light response speeds and stabilities. The I_{ph} is in descending order of TSO-0.7 > TSO-0.5 > TSO-0.3 under both UV and visible-light illumination, and corresponding well with the photocatalytic activity. In particular, TSO-0.7 solid solution under artificial light illumination shows the highest photocurrent among all the samples. This prominent enhancement of photocurrent for TSO-0.7 mainly results from its suitable band gap structure (larger light harvesting) and the presence of structural vacancies.

The electrochemical impedance spectroscopy (EIS) Nyquist plot is a powerful tool to reveal the interface properties between solutions and electrodes. The radius of the circular arc in the EIS Nyquist plot corresponds to the separation efficiency of the photogenerated electron–hole pairs and the charge transfer resistance [79]. The arc radius decreases with increasing Ti:Sn ratio and varies in the following sequence: TSO-0.3 > TSO-0.5 > TSO-0.7 (Fig. 12). The result corresponds very well with the observations in the photocatalytic activity tests and the chronoamperometry analyses.

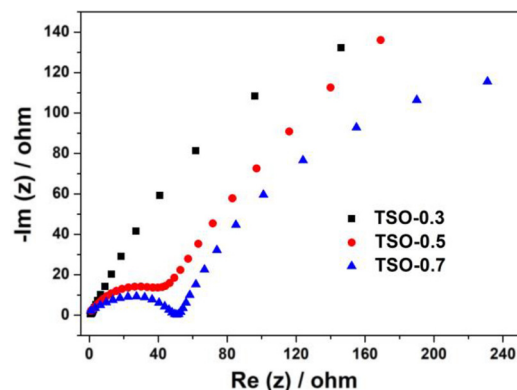


Fig. 12. Nyquist impedance plots of TSO-x ($x = 0.3, 0.5, 0.7$) samples in 0.2 M $[Fe(CN)_6]^{3-}/[Fe(CN)_6]^{4-}$ solution with 200 mV bias versus Ag/AgCl electrodes.

3.7. Tentative mechanism for the photocatalytic process of TSO samples

Accordingly, based on the above discussion about the chemical and electric structure and photoelectric properties of TSO solid solutions, the excellent photocatalytic performance of the core-shell TSO solid solutions is attributable to the synergistic effect of their unique morpho-structure, energy band position, light-absorption capacity, and surface absorbed hydroxyl groups. A tentative mechanism for the photochemical processes is elucidated in Scheme 2. Under irradiation, the

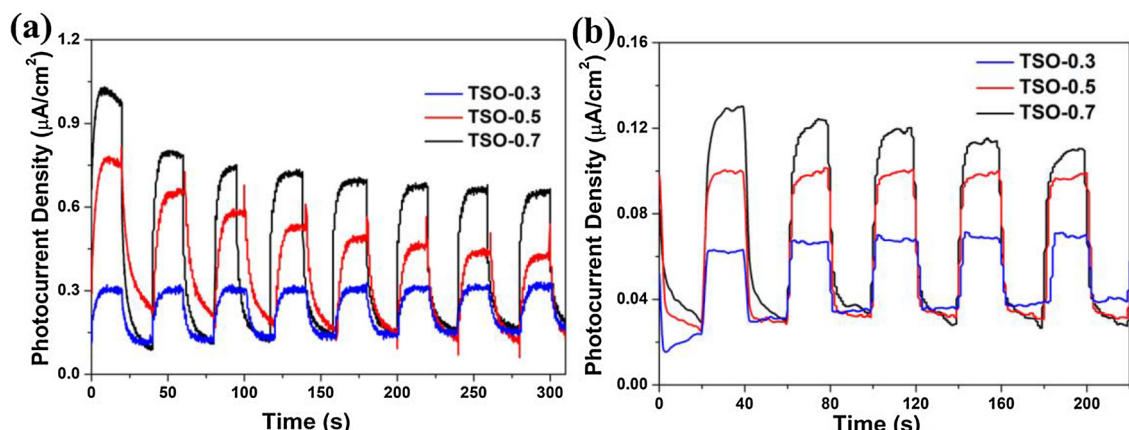
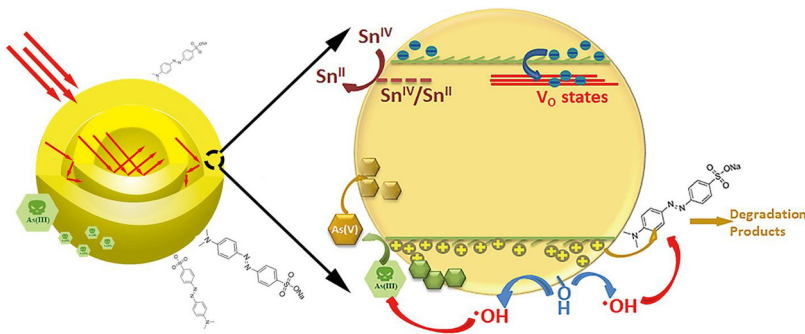


Fig. 11. Transient photocurrent responses of the TSO-x ($x = 0.3, 0.5$ and 0.7) samples with 0.2 V bias versus Ag/AgCl electrodes in 0.2 M Na_2SO_4 solution under (a) UV and (b) visible light irradiation.



Scheme 2. Schematic diagram of the mechanism for photo-oxidation of MO or As(III) over the TSO solid solutions nanoparticles under irradiation.

core-shell structure of TSO solid solutions allows the entrance and multiple reflection of light in the interior cavity, resulting in more efficient use of the light source. Due to its high specific surface areas, moreover, the H_2O molecule (dissociated as hydroxyl groups), and the pollutants such as dye molecules and As(III) species can readily adsorbed onto the surface of core-shell TSO solid solutions. One the other hand, the suitable energy band position also endow the photocatalysts a strong light absorption for the excitation light. The excited photo-generated holes on the valence band can react with adsorbed pollutants or hydroxyl groups to initiate the photocatalytic oxidation process. The electrons on the conduction band (CB), are unable to reduce oxygen because the CB position of TSO solid solutions is lower than the standard redox potential of the redox system O_2/O_2^- . Nevertheless, the excited electrons can react with Sn^{4+} ions alternatively for the suitable redox potentials of $\text{Sn}^{\text{IV}}/\text{Sn}^{\text{II}}$ couples. The existence of structural defects such as oxygen vacancies (V_0) can act as shallow traps for electrons. Both two factors can account for the enhanced electron–hole pair separation efficiency. Thus, in our TSO-pollutants system, the high active and long-lived holes (h_{VB}^+) are readily achieved and play a crucial role in the photocatalysis process.

4. Conclusion

In summary, applying $\text{SnCl}_4 \cdot 5\text{H}_2\text{O}$ and Titanium butoxide as the precursors, porous core-shell $\text{Ti}_x\text{Sn}_{1-x}\text{O}_2$ solid solutions with highly broad-light active have been successfully fabricated via a mild one-pot solvothermal route. The solid solutions in the whole range ($x = 0.0\text{--}1.0$) can be effectively achieved by control the Ti:Sn molar ratios. The experimental analyses highlighted that the physical Ostwald ripening process coupled with chemical conversion could induce the self-development of core-shell $\text{Ti}_x\text{Sn}_{1-x}\text{O}_2$ solid solution. The $\text{Ti}_x\text{Sn}_{1-x}\text{O}_2$ solid solutions are of small crystallite sizes and their XRD patterns match very well with the standard patterns in the database. The combination of TiO_2 and SnO_2 at atomic level can extend the photo-response to the visible region. The unique core-shell porous morphostructure, high specific surface area and controllable band structure further endow the TSO solid solutions with excellent photocatalytic activity. When the Ti:Sn molar ratio is 7:3, $\text{Ti}_{0.7}\text{Sn}_{0.3}\text{O}_2$ (TSO-0.7) microspheres show the highest photocatalytic activity for MO degradation and As(III) oxidation. The enhancement can be attributed predominantly to the high light-harvesting capacity and effective photo-generated charge separation of the TSO solid solutions. The photo-generated holes and $\cdot\text{OH}$ radicals are the main responsive active species for the photocatalysis process in the TSO-pollutants systems. As the core-shell $\text{Ti}_x\text{Sn}_{1-x}\text{O}_2$ solid solutions have the advantages of simple synthesis, unique morphostructure and excellent photoelectric properties, wide applications in catalysis, gas sensors, separation technology, biomedical engineering and nanotechnology are expected.

Acknowledgements

This work is financially supported by National Natural Science Foundation of China (Nos. 21303244 and 21673044), Program for New Century Excellent Talents in Fujian Province University (NCETFJ), Natural Science Foundation of Fujian Province (No. 2016J01207), and Outstanding Youth Fund of Fujian Agriculture and Forestry University (No. XJQ201419).

Appendix A. Supplementary data

Supplementary material related to this article can be found, in the online version, at doi:<https://doi.org/10.1016/j.apcatb.2018.11.045>.

References

- [1] A. Fujishima, K. Honda, *Nature* 238 (1972) 37–38.
- [2] M.R. Hoffmann, S.T. Martin, W. Choi, D.W. Bahnemann, *Chem. Rev.* 95 (1995) 69–96.
- [3] D.S. Bhatkhande, V.G. Pangarkar, A.A.C.M. Beenackers, *J. Chem. Technol. Biotechnol.: Int. Res. Process Environ. Clean Technol.* 77 (2002) 102–116.
- [4] W.-J. Ong, L.-L. Tan, Y.H. Ng, S.-T. Yong, S.-P. Chai, *Chem. Rev.* 116 (2016) 7159–7329.
- [5] A. Di Paola, E. García-López, G. Marci, L. Palmisano, *J. Hazard. Mater.* 211 (2012) 3–29.
- [6] Z. Wan, G. Zhang, X. Wu, S. Yin, *Appl. Catal. B* 207 (2017) 17–26.
- [7] Y.-L. Zhang, J. Yang, X.-J. Yu, *Rare Met.* 36 (2017) 987–991.
- [8] M. Pelaez, N.T. Nolan, S.C. Pillai, M.K. Seery, P. Falaras, A.G. Kontos, P.S. Dunlop, J.W. Hamilton, J.A. Byrne, K. O'shea, *Appl. Catal. B* 125 (2012) 331–349.
- [9] X. Chen, C. Burda, *J. Am. Chem. Soc.* 130 (2008) 5018–5019.
- [10] J. Zhuang, W. Dai, Q. Tian, Z. Li, L. Xie, J. Wang, P. Liu, X. Shi, D. Wang, *Langmuir* 26 (2010) 9686–9694.
- [11] J. Sun, K. Zhu, F. Gao, C. Wang, J. Liu, C.H. Peden, Y. Wang, *J. Am. Chem. Soc.* 133 (2011) 11096–11099.
- [12] W.Y. Hernández, M.A. Centeno, F. Romero-Sarria, J.A. Odriozola, *J. Phys. Chem. C* 113 (2009) 5629–5635.
- [13] X. Yao, Y. Xiong, W. Zou, L. Zhang, S. Wu, X. Dong, F. Gao, Y. Deng, C. Tang, Z. Chen, *Appl. Catal. B* 144 (2014) 152–165.
- [14] M.V. Dozzi, S. Marzorati, M. Longhi, M. Coduri, L. Artiglia, E. Sellì, *Appl. Catal. B* 186 (2016) 157–165.
- [15] K. Zakrzewska, *Thin Solid Films* 391 (2001) 229–238.
- [16] A. Kusior, J. Klich-Kafel, A. Trenck-Zajac, K. Swierczek, M. Radecka, K. Zakrzewska, *J. Eur. Ceram. Soc.* 33 (2013) 2285–2290.
- [17] S. Li, M. Ling, J.X. Qiu, J.S. Han, S.Q. Zhang, *J. Mater. Chem. A Mater. Energy Sustain.* 3 (2015) 9700–9706.
- [18] K. Maeda, T. Takata, M. Hara, N. Saito, Y. Inoue, H. Kobayashi, K. Domen, *J. Am. Chem. Soc.* 127 (2005) 8286–8287.
- [19] L. Xu, Y. Su, S. Li, Y. Chen, Q. Zhou, S. Yin, Y. Feng, *J. Phys. Chem. B* 111 (2007) 760–766.
- [20] Q. Li, H. Meng, P. Zhou, Y.Q. Zheng, J. Wang, J.G. Yu, J.R. Gong, *ACS Catal.* 3 (2013) 882–889.
- [21] M. Kaur, C.M. Nagaraja, *ACS Sustain. Chem. Eng.* 5 (2017) 4293–4303.
- [22] W.J. Fang, Z. Jiang, L. Yu, H. Liu, W.F. Shangguan, C. Terashima, A. Fujishima, *J. Catal.* 352 (2017) 155–159.
- [23] M.C. Carotta, S. Gherardi, V. Guidi, C. Malagu, G. Martinelli, B. Vendemiat, M. Sacerdoti, G. Ghiootti, S. Morandi, *Thin Solid Films* 517 (2009) 6176–6183.
- [24] J. Lin, J.C. Yu, D. Lo, S.K. Lam, *J. Catal.* 183 (1999) 368–372.
- [25] M. Park, T.E. Mitchell, A.H. Heuer, *J. Am. Ceram. Soc.* 58 (1975) 43–47.
- [26] H. Uchiyama, H. Imai, *Chem. Commun.* (2005) 6014–6016.
- [27] M.M. Oliveira, D.C. Schnitzler, A.J.G. Zarbin, *Chem. Mater.* 15 (2003) 1903–1909.
- [28] Y. Cao, W. Yang, W. Zhang, G. Liu, P. Yue, *New J. Chem.* 28 (2004) 218–222.
- [29] L. Dong, Y.X. Tang, B. Li, L.Y. Zhou, F.Z. Gong, H.X. He, B.Z. Sun, C.J. Tang, F. Gao,

[31] L. Dong, *Appl. Catal. B* 180 (2016) 451–462.

[30] Y. Zhao, J. Liu, L. Shi, S. Yuan, J. Fang, Z. Wang, M. Zhang, *Appl. Catal. B* 100 (2010) 68–76.

[31] L. Trottochaud, S.W. Boettcher, *Chem. Mater.* 23 (2011) 4920–4930.

[32] L.B. Kong, J. Ma, H. Huang, *J. Alloys Compd.* 336 (2002) 315–319.

[33] K. Asokan, J.Y. Park, S. Choi, C. Chang, S.S. Kim, *Nano Res.* 3 (2010) 256–263.

[34] K. Zakrzewska, M. Radecka, *Procedia Eng.* 47 (2012) 1077–1080.

[35] W. Zeng, T.M. Liu, Z.C. Wang, S. Tsukimoto, M. Saito, Y. Ikuhara, *Sensors-Basel* 9 (2009) 9029–9038.

[36] N.R. Srinivasan, R. Bandyopadhyaya, *Faraday Discuss.* 186 (2016) 353–370.

[37] J.Y. Jung, S. Cho, Y.S. Lee, *J. Alloys Compd.* 614 (2014) 310–316.

[38] H.K. Wang, H. Huang, C.M. Niu, A.L. Rogach, *Small* 11 (2015) 1364–1383.

[39] Y. Yin, R.M. Rioux, C.K. Erdonmez, S. Hughes, G.A. Somorjai, A.P. Alivisatos, *Science* 304 (2004) 711–714.

[40] F. Caruso, R.A. Caruso, H. Möhwald, *Science* 282 (1998) 1111–1114.

[41] X.W. Lou, L.A. Archer, Z. Yang, *Adv. Mater.* 20 (2008) 3987–4019.

[42] Z.W. Seh, W. Li, J.J. Cha, G. Zheng, Y. Yang, M.T. McDowell, P. Hsu, Y. Cui, *Nat. Commun.* 4 (2013) 1331.

[43] L.J. Lauhon, M.S. Gudiksen, D. Wang, C.M. Lieber, *Nature* 420 (2002) 57.

[44] R. Shi, Y. Cao, Y. Bao, Y. Zhao, G.I. Waterhouse, Z. Fang, L.Z. Wu, C.H. Tung, Y. Yin, T. Zhang, *Adv. Mater.* 29 (2017) 1700803.

[45] S.B. Yoon, K. Sohn, J.Y. Kim, C.H. Shin, J.S. Yu, T. Hyeon, *Adv. Mater.* 14 (2002) 19–21.

[46] J. Liu, S.Z. Qiao, S. Budi Hartono, G.Q. Lu, *Angew. Chemie Int. Ed.* 49 (2010) 4981–4985.

[47] Y. Chen, H. Chen, D. Zeng, Y. Tian, F. Chen, J. Feng, J. Shi, *ACS Nano* 4 (2010) 6001–6013.

[48] Q. Zhang, I. Lee, J.B. Joo, F. Zaera, Y. Yin, *Acc. Chem. Res.* 46 (2012) 1816–1824.

[49] W.H. Suh, A.R. Jang, Y.H. Suh, K.S. Suslick, *Adv. Mater.* 18 (2006) 1832–1837.

[50] Y. Qu, X. Duan, *Chem. Soc. Rev.* 42 (2013) 2568–2580.

[51] H. Li, Z. Bian, J. Zhu, D. Zhang, G. Li, Y. Huo, H. Li, Y. Lu, *J. Am. Chem. Soc.* 129 (2007) 8406–8407.

[52] J. Zhuang, Q. Tian, H. Zhou, Q. Liu, P. Liu, H. Zhong, *J. Mater. Chem.* 22 (2012) 7036–7042.

[53] D. Tang, J. Li, G. Zhang, *Appl. Catal. B* 224 (2018) 433–441.

[54] Y. Sun, B.T. Mayers, Y. Xia, *Nano Lett.* 2 (2002) 481–485.

[55] X. Sun, Y. Li, *Angew. Chemie Int. Ed.* 116 (2004) 607–611.

[56] F. Caruso, *Chem. Eur. J.* 6 (2000) 413–419.

[57] H.G. Yang, H.C. Zeng, *J. Phys. Chem. B* 108 (2004) 3492–3495.

[58] B. Liu, H.C. Zeng, *Small* 1 (2005) 566–571.

[59] X.M. Yin, C.C. Li, M. Zhang, Q.Y. Hao, S. Liu, L.B. Chen, T.H. Wang, *J. Phys. Chem. C* 114 (2010) 8084–8088.

[60] Q. Zhang, W. Wang, J. Goebel, Y. Yin, *Nano Today* 4 (2009) 494–507.

[61] K.-S. Kim, *Chem. Eng. J.* 286 (2016) 266–271.

[62] J. Li, H.C. Zeng, *J. Am. Chem. Soc.* 129 (2007) 15839–15847.

[63] J. Yu, S. Liu, M. Zhou, *J. Phys. Chem. C* 112 (2008) 2050–2057.

[64] F.R. Sensato, R. Custodio, E. Longo, A. Beltran, J. Andres, *Catal. Today* 85 (2003) 145–152.

[65] P. Chetri, P. Basyach, A. Choudhury, *Chem. Phys.* 434 (2014) 1–10.

[66] M.H. Harunsani, F.E. Oropeza, R.G. Palgrave, R.G. Eggle, *Chem. Mater.* 22 (2010) 1551–1558.

[67] F.E. Oropeza, B. Mei, I. Sinev, A.E. Becerikli, M. Muhler, J. Strunk, *Appl. Catal. B* 140 (2013) 51–59.

[68] F. Sayilan, M. Asiltürk, P. Tatar, N. Kiraz, S. Şener, E. Arpaç, H. Sayilan, *Mater. Res. Bull.* 43 (2008) 127–134.

[69] B. Choudhury, A. Choudhury, *Curr. Appl. Phys.* 13 (2013) 217–223.

[70] R. Long, Y. Dai, B. Huang, *J. Phys. Chem. C* 113 (2008) 650–653.

[71] R.G. Pearson, *Inorg. Chem.* 27 (1988) 734–740.

[72] M. Batzill, U. Diebold, *Prog. Surf. Sci.* 79 (2005) 47–154.

[73] J. Li, J. Wang, G. Zhang, Y. Li, K. Wang, *Appl. Catal. B* 234 (2018) 167–177.

[74] C. Zhou, Y. Zhao, L. Shang, Y. Cao, L.-Z. Wu, C.-H. Tung, T. Zhang, *Chem. Commun.* 50 (2014) 9554–9556.

[75] J. Zhuang, Q. Tian, Q. Liu, P. Liu, X. Cui, Y. Li, M. Fan, *J. Chem. Soc. Faraday Trans.* 19 (2017) 9519–9527.

[76] A. Bard, R. Parsons, J. Jordan, Marcel Dekker, New York (1985) 843.

[77] J. Zhuang, Q. Tian, P. Liu, *Acta Phys. Sin.* 32 (2016) 551–557.

[78] J. Zhuang, Q. Tian, S. Lin, W. Yang, L. Chen, P. Liu, *Appl. Catal. B* 156 (2014) 108–115.

[79] J.W. Ondersma, T.W. Hamann, *Langmuir* 27 (2011) 13361–13366.